Surface electronic structure of Ni-doped Fe_3O_4(001)

Mert Taskin,[1] Zbynek Novotny,[1,2,3] Nicolo Comini,[1,2] J. Trey Diulus,[1,2] Matthias Hengsberger,[1] Peter Krüger,[4] and Jürg Osterwalder[1,*]

[1]*Physik-Institut, Universität Zürich, Winterthurerstrasse 190, CH-8057 Zürich, Switzerland*

[2]*Swiss Light Source, Paul Scherrer Institut, CH-5232 Villigen, Switzerland*

[3]*EMPA, Laboratory for Joining Technologies and Corrosion, Swiss Federal Laboratories for Materials, CH-8600 Dübendorf, Switzerland*

[4]*Graduate School of Advanced Integration Science, Chiba University, 263-8522 Chiba, Japan*

(Received 24 May 2023; accepted 30 August 2023; published 2 October 2023)

Magnetite (Fe_3O_4) doped with earth-abundant metals has emerged as a promising catalyst material, with Ni-doped magnetite (Ni/Fe_3O_4) being a cost-effective, durable, and highly active material for photocatalytic and electrochemical water oxidation. While previous studies have investigated the incorporation of Ni atoms into Fe_3O_4 single-crystalline surfaces using surface science characterization methods and density functional theory calculations, an experimental study is still required to understand the impact of Ni incorporation on the electronic structure of Ni/Fe_3O_4 systems. To address this, we employed angle-resolved photoemission spectroscopy, analyzed within the one-step model of photoemission by a real-space multiple scattering code to investigate the electronic structure of the reconstructed magnetite surface. Moreover, the half-metal to semiconductor phase transition upon Ni incorporation is reflected in an almost complete disappearance of states near the Fermi level. Finally, we report on the systematic changes in the unoccupied states observed with the increasing amount of Ni dopant. These findings offer insights into the influence of Ni incorporation on the electronic structure of Ni/Fe_3O_4, which can link to an increased catalytic activity.

DOI: 10.1103/PhysRevB.108.155403

I. INTRODUCTION

Magnetite (Fe_3O_4) is the oldest magnetic material known to humankind, discovered around 1500 BC. Recently, Fe_3O_4 became a very interesting system in other fields of studies, such as spintronics and electronic phase transitions, due to its ferrimagnetic and/or half-metallic nature [1–5]. The electronic structure of Fe_3O_4 has attracted attention as it undergoes an insulator to half-metallic phase transition at $T_V \approx 120$ K, the so-called Verwey transition [6]. Below T_V, Fe_3O_4 crystallizes in a low-symmetry monoclinic structure ($C2/c$) [7,8]. This is reflected in the electronic structure as charge and orbital ordering within octahedrally coordinated sites, associated with the enhanced interaction between 3d electrons due to the strong Coulomb potential, and in the subsequent distortions in the lattice [8–10]. Heating through the Verwey transition results in an increase in electrical conductivity by two orders of magnitude [11], along with a crystal structure transformation into an inverse spinel structure ($Fd\bar{3}m$), where Fe_3O_4 is composed of three inequivalent Fe cations in the lattice: Fe^{3+}_{oct} and Fe^{2+}_{oct} in octahedrally coordinated sites, and Fe^{3+}_{tet} in tetrahedral sites. The crystal is considered to be a half-metal due to charge hopping within the octahedrally coordinated cation sublattice. There is no allowed electronic hopping between Fe_{tet} and Fe_{oct} atoms due to their antiferromagnetically aligned spins [1].

According to crystal field theory, the two different coordinations of Fe ions in the Fe_{oct} and Fe_{tet} sublattices induce the 3d shell to split into t_{2g}/e_g and t_2/e subbands, respectively, as described for the inverse spinel-type transition-metal oxides [12,13]. Note that e and t imply double and triple degeneracy, respectively, while the g index ("gerade") stands for inversion symmetry which is lifted for Fe_{tet} sites. The electronic structure of the multivalent Fe 3d shell was studied with resonant [14,15], spin-resolved [4,16,17], and angle-resolved [18,19] photoelectron spectroscopy as well as band structure calculations within the local spin density approximation (LSDA) [1,3], local density approximation (LDA) [20], and generalized gradient approximation (GGA) [18]. The experimental results suggested that the Fe^{2+}_{oct} $\downarrow$ electrons ($\downarrow$: minority spin), which were reported to occupy a t_{2g} band with a band bottom at $\approx$0.5 eV [21] or $\approx$0.8 eV [18] below E_F, are responsible for the electrical conduction. The exact assignment of the conduction band, however, remains challenging due to the strong correlation effects that emerge with many-body interactions, in particular, electron-phonon and electron-magnon scattering [21–24].

Surfaces of cubic phase Fe_3O_4 can be functionalized by doping with transition metals (M), forming $M_xFe_{3-x}O_4$ phases that have attracted attention as efficient and earth-abundant catalysts for water oxidation [25–27]. Of particular interest is the Fe_3O_4(001) surface that can appear in two different surface terminations: (i) the bulk-truncated (1 × 1) surface and (ii) a $(\sqrt{2} \times \sqrt{2})$-$R45°$ reconstruction. The presence

*osterwal@physik.uzh.ch

of the reconstruction was attributed to the coexistence of two subsurface cation vacancies in the octahedral sites in the third subsurface layer (S-2) and one interstitial cation in a tetrahedral site of the second layer (S-1), a structure termed the subsurface cation vacancy (SCV) reconstruction [20]. Reorganization of cations near the surface distorts the octahedral lattice in the topmost layer, resulting in an undulation effect in the surface Fe and O rows. This influences the adsorption coordination of guest cations, and defines energetically favorable pathways for their incorporation into the subsurface. The adsorption and incorporation mechanism of guest 3*d* cations such as Ni [26,28–30], among others [31] on the $Fe_3O_4(001)$ model system, were investigated widely with surface characterization methods. Particularly, the presence of Ni dopants in the Fe_3O_4 surface region was found to significantly enhance its reactivity to water [25,32,33], where the amount of incorporated Ni near the surface was found to be a tuning parameter for the efficiency of the oxygen evolution reaction [26]. Theoretical results suggest that a defect-free $NiFe_2O_4(001)$ surface favors the adsorption of water molecules on Ni cations, although they dissociate on neighboring Fe cations resulting in the formation of Fe-OH bonds and H bonding with surface oxygen [33]. The fact that initial water adsorption is governed by surface Ni sites shows the importance of the Ni density near the Fe_3O_4 surface.

LDA + U calculations showed that the Ni dopants tend to occupy octahedral sites in the sublattice, while Ni occupation in the tetrahedral sites was reported to be energetically unfavored [29]. The incorporated Ni ions have a 2+ charge state, as they substitute for Fe^{2+}_{oct} to form ideal nickel-ferrite $Ni_xFe_{3-x}O_4$ ($x = 1$). The density of states (DOS) of $NiFe_2O_4$ near E_F was investigated with various computational [33–36] and experimental [37,38] methods which showed that the spin configuration of the two sublattices remains antiferromagnetically aligned after Fe^{2+}_{oct} is replaced by Ni^{2+}_{oct}. The extra two electrons from Ni^{2+} fill the t_{2g} band near E_F, resulting in a gap in the band structure. The electronegativity difference between Fe^{2+} and Ni^{2+} shifts the t_{2g} band deeper below E_F, thus supporting the band-gap opening. Different values for the band gap are reported in the literature ranging from 0.33 eV to approximately 3 eV for $NiFe_2O_4$ [35,39–42]. In order to gain further insight into electronic states of Ni-doped Fe_3O_4 systems, relevant for the catalytic activity, we first focused on the electrons populating the t_{2g} band of the bare $(\sqrt{2} \times \sqrt{2})$-$R45^\circ$ reconstructed $Fe_3O_4(001)$ surface by exploiting angle-resolved ultraviolet photoelectron spectroscopy (ARUPS). Emission intensities at fixed initial-state energy E_i are mapped as a function of $\vec{k}_\parallel$, investigated with ultraviolet photoelectron diffraction (UPD) effects. Two different excitation energies were employed to distinguish photoelectron scattering, which emerge as a final-state effect. The data are compared to simulations using a real-space multiple scattering method [43]. Furthermore, we examine the changes induced in the occupied states by the incorporation of Ni ions into the $Fe_3O_4(001)$ surface. Finally, we report systematic changes in the unoccupied states of $Ni/Fe_3O_4(001)$ as a function of the Ni concentration, observed with x-ray absorption near edge structure (XANES).

II. EXPERIMENTAL DETAILS

Naturally occurring and polished $Fe_3O_4(001)$ single crystals purchased from SurfaceNet GmbH were used in the photoemission and low-energy electron diffraction (LEED) measurements. To obtain the reconstructed surface, the $Fe_3O_4(001)$ samples were prepared with two cycles of Ar^+ sputtering with a mean kinetic energy $U_{mean} \approx 1$ kV (10 min) and annealing ($T = 950$ K) under an oxygen pressure of $p_{O_2} = 5 \times 10^{-7}$ mbar (20 min). After the sample preparation, the surface reconstruction was confirmed with LEED measurements (Scienta Omicron LEED). Detailed information about sample preparation of Ni-doped $Fe_3O_4(001)$, as well as its structural characterization, Ni incorporation kinetics, and compositional quantification, is given in Ref. [28].

The samples for the synchrotron experiments were prepared in a separate UHV chamber with a base pressure of 2×10^{-10} mbar. Here, the sample preparation consisted of cycles of Ar^+ sputtering (mean kinetic energy of 950 eV, 30 min) and annealing alternating exposure to 5×10^{-7} mbar of molecular O_2 for 10 min, and UHV annealing at 1100 K for 15 min. The $(\sqrt{2} \times \sqrt{2})$-$R45^\circ$ structure was verified by LEED. Ni was deposited on the $Fe_3O_4(001)$ samples kept at 607 K from a 2-mm-thick Ni wire (Alfa Aesar, 99.999%) using an electron beam evaporator (EFM3, Focus GmbH) calibrated with a water-cooled quartz crystal microbalance (Inficon) placed at the same position as the sample during evaporation. For consistency with earlier work [44], the monolayer (1 ML $\approx 1.4 \times 10^{14}$ cm^{-2}) coverage of Ni was defined as one Ni atom per surface unit-cell area (8.44×8.44 Å^2). Different growth methods have been employed for the data sets shown below in Secs. IV B and IV C. In Sec. IV B, depositing 26 ML of Ni on the $Fe_3O_4(001)$ surface at 473 K followed by a postannealing at 607 K overnight (≈12 h) resulted in a composition of $x = 2$ in $Ni_xFe_{3-x}O_4(001)$ in the near-surface region of the crystal [28].

For the experiments described in Sec. IV C, Ni atoms were deposited on $Fe_3O_4(001)$ with coverages of 10, 50, and 120 ML, reached after 0.08, 0.4, and 0.96 h of constant evaporation rate, respectively, at a substrate temperature of 607 K. No postannealing was done. Based on our previous temperature-dependent XPS measurements [28] we know that, even at 607 K, the Ni incorporation kinetics are slow with respect to the applied evaporation rate once the content of incorporated Ni in the $Ni_xFe_{3-x}O_4(001)$ has reached $x = 1$ within the XPS probing depth. The latter is the case for the 10-ML sample where all Ni atoms are incorporated in the lattice (see Sec. IV B). For longer deposition times this supersaturation leads to the accumulation of excess Ni^0 on the surface in the form of metallic clusters, and the formation of a ferrite phase with $x > 1$, with x depending on the deposition time rather than on the overall amount of deposited Ni. In Ref. [28], it was found that values of nearly $x = 2$ could be reached after postannealing at 607 K for approximately 12 h. In the case of the present 50- and 120-ML samples, considerable amounts of Ni^0 remained on the surface, making a reliable quantification of x by XPS impossible. Yet, based on the deposition times we can ascertain that $1 < x(50\ \text{ML}) < x(120\ \text{ML}) < 2$, with values of x rather close to 1 due to the short deposition times.

Photoemission measurements in our home laboratory [45] were conducted in a modified VG ESCALAB 220 UHV system with a base pressure of 2.1×10^{-10} mbar. The core-level electrons were excited with nonmonochromatized Mg K_α ($\hbar\omega = 1253.6$ eV) radiation from a twin anode x-ray source. The Auger electron diffraction (AED) pattern was obtained by measuring the angular intensity distribution of the Ni LMM Auger line. This pattern was recorded with Si K_α ($\hbar\omega = 1740$ eV) excitation, as a function of azimuthal ($\phi = 0^\circ$ to 360°) and polar angles ($\theta = 80^\circ$ to 0°) at constant kinetic energy after the subtraction of the inelastic background [46,47]. In addition, a Gaussian-shaped polar background was subtracted from the pattern to account for purely instrumental intensity variations. Fourfold symmetrical rotational averaging was applied to the pattern to improve the statistical accuracy, but all features were also clearly visible in the nonsymmetrized data. A microwave-driven high-flux monochromatized He discharge lamp (He I_α, $\hbar\omega = 21.22$ eV and He II_α, $\hbar\omega = 40.8$ eV) was used for the valence band measurements (Gammadata Burklint AB, Sweden). The monochromatized UV source has a partially linearly polarization (see Fig. SI1 [48]). Constant-energy angular maps of valence band states were measured using this UV source and applying the same angular mapping procedure as for the AED pattern. Since final-state scattering appears to be the dominant effect producing these patterns, they will be referred to as ultraviolet photoelectron diffraction (UPD) patterns. Note that all the measurements discussed in Secs. IV A and IV B were acquired with laboratory-based light sources.

The experiments for XANES and XPS measurements discussed in Sec. IV C were conducted at the In-Situ Spectroscopy (X07DB) beamline of the Swiss Light Source (SLS), using the Solid-Liquid Interface Chamber (SLIC) end-station [49]. X-ray photoelectron spectra were at a base pressure below 1×10^{-8} mbar, using a Scienta R4000 HiPP-2 analyzer with an entrance cone aperture diameter of 500 μm and a working distance of 1 mm, operated in a transmission lens mode using 20-eV pass energy. The high background pressure as compared to UHV conditions results in the formation of approximately half of a dense monolayer of C contamination during the measurements. We carefully checked by comparing with measurements taken under UHV conditions that the contamination did neither influence the line shapes nor the relevant intensity ratios. Sample heating during Ni deposition was performed with resistive heating, and the temperature was determined using a Pt100 sensor [49]. The XANES measurements presented in Sec. IV C were taken with synchrotron radiation, with a monochromator that was not precisely calibrated to better than 2 eV in absolute photon energies. Since the main focus is to demonstrate the changes in relative peak positions and intensities within the Ni $L_{2,3}$ [37], Fe $L_{2,3}$ [50], and O K [51] edges, they are presented with an energy offset to match prior studies in the literature.

III. COMPUTATIONAL DETAILS

The reconstructed $Fe_3O_4(001)$ surface was modeled using a 17 atomic-layer slab (see Fig. SI2 [48]) with atomic positions known from experiment [20]. All calculations were done in the local density approximation (LDA) or the LDA + U approach with $U_{\text{eff}} \equiv U - J = 3.8$ eV for the Fe-3d states [20]. The surface electronic structure and projected density of states (PDOS) were computed with the projector-augmented-wave code VASP [52,53] using an energy cutoff of 400 eV. For the photoemission calculations, we used the finite-cluster real-space multiple scattering (RSMS) method by Krüger *et al.* [43]. The method needs atomic potentials which were generated in a Fe_3O_4 bulk calculation with the LMTO code [54]. We verified that the LMTO and VASP band structures are indeed similar. Moreover, the PDOS obtained in RSMS for the inner atoms of a bulklike Fe_3O_4 cluster (439 atoms) agrees very well with the PDOS of the infinite crystal as computed with VASP or LMTO.

We also calculated the LDA + U band structure of $Ni_xFe_{3-x}O_4$ ($x = 1, 2$) bulk with Ni substituting Fe cations in octahedral sites. As for Fe_3O_4, the VASP code was used with $U_{\text{eff}} = 3.8$ eV for Fe and $U_{\text{eff}} = 4.8$ eV for Ni [33]. We assumed that the Ni atoms have the same spin orientation as Fe at octahedral sites.

$E(\vec{k}_\parallel)$ band dispersions were investigated along with photoelectron diffraction effects for UV (He I_α and He II_α) excitation energies. For photons with energy $\hbar\omega$ and polarization ϵ, the photoemission intensity according to the one-step model is given by

$$I(\omega, \epsilon, \vec{k}) = \sum_v |\langle \psi_k | D_\epsilon | \psi_v \rangle|^2 \delta(E_k - E_v - \hbar\omega), \quad (1)$$

where $|\psi_v\rangle$ denotes a valence state with energy E_v and D_ϵ is the electric dipole operator. The photoemission final states $|\psi_k\rangle$ have energy E_k and are detected with momentum $\vec{k}$. They obey time-reversed LEED boundary conditions, i.e., far from the surface, the wave function is given by

$$|\psi_k\rangle = \exp(i\vec{k} \cdot \vec{r}) + \sum_A f_A \exp(ikr_A)/r_A, \quad (2)$$

where the first term is a plane wave and the second term the sum of the scattered, spherical waves, incoming onto some atom A at position $\vec{R}_A$. Furthermore, $r_A \equiv |\vec{r} - \vec{R}_A|$ and f_A is the scattering amplitude, which takes into account multiple scattering events to infinite order in the cluster [43]. The RSMS method is used for both initial and final states. Semiellipsoidal clusters of three different sizes were tested, both for the bulk-terminated (1×1) and the reconstructed $(\sqrt{2} \times \sqrt{2})$-$R45^\circ$ surface terminations. A 448-atom cluster model of the reconstructed surface (see Fig. SI2 [48]) gave best agreement with the measured UPD patterns.

Additionally, the electron diffraction in atomic clusters (EDAC) code [55] was used to generate simulations of XPD patterns. For these simulations, atomic clusters were set up that represent the bulk-truncated (1×1) structure along a (001) plane. To compare to the findings from the Ni LMM Auger diffraction data, layer-resolved XPD patterns were simulated for Fe $2p_{3/2}$ by selectively considering Fe emitters either on the surface or within the (S-n)th subsurface layer, but using the kinetic energy of the Ni LMM Auger line (840 eV) [28].

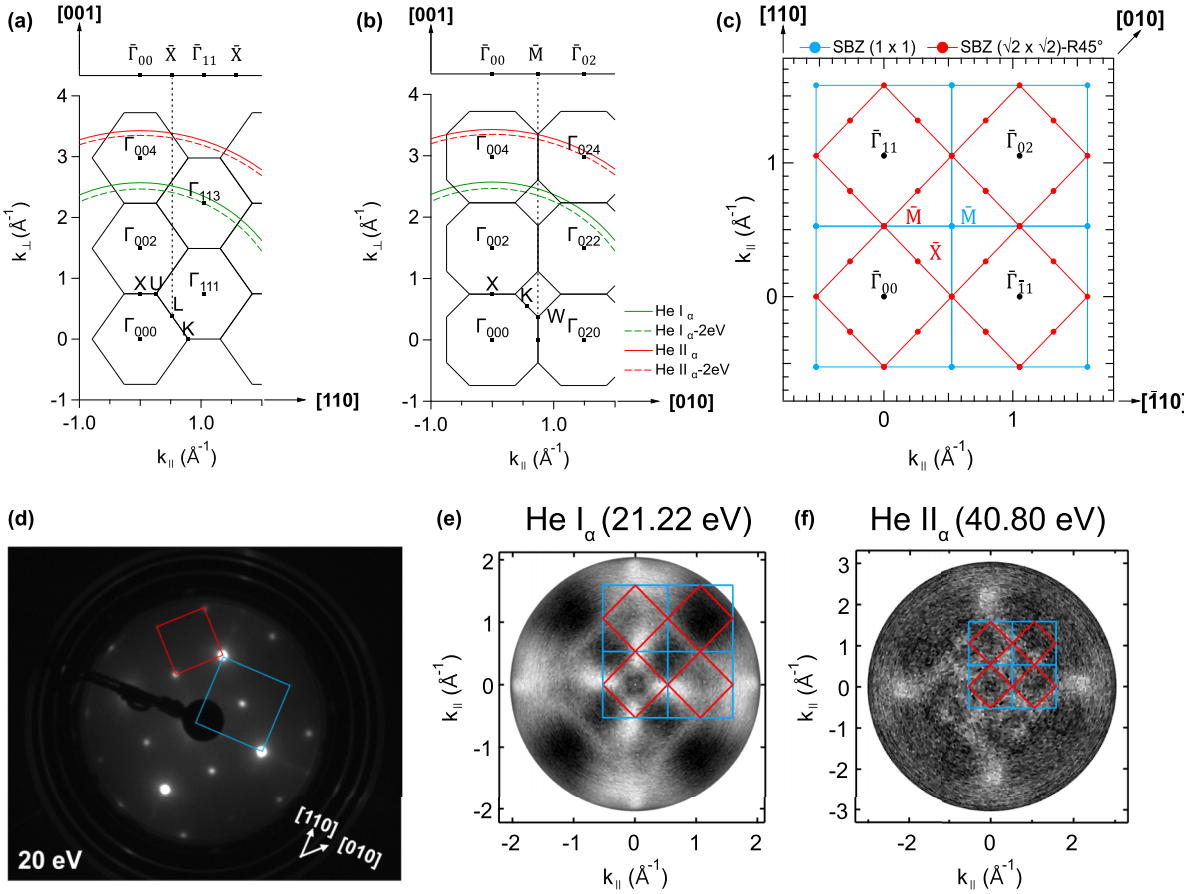

FIG. 1. (a), (b) Sections through the bulk BZ boundaries within the [110] and [010] planes. Green and red lines represent the free-electron final states covered by ARUPS measurements with He I_α and He II_α excitation, respectively. The solid and dashed lines represent the final states for electrons with initial states at 0-eV (E_F) and 2-eV binding energy, respectively. (c) SBZ boundaries projected from the bulk BZ given in (a) and (b) for (1 × 1) (blue squares), and for the reconstructed surface (red squares). High-symmetry points for the latter are indicated. (d) LEED image taken at 20 eV, and Fermi-surface maps (FSM) acquired with (e) He I_α and (f) He II_α on the $(\sqrt{2} \times \sqrt{2})$-$R45^\circ$ reconstructed $Fe_3O_4(001)$ surface given with overlaid reciprocal cells. A fourfold symmetry averaging was applied to each FSM.

IV. RESULTS AND DISCUSSION

This part is organized as follows: In Sec. IV A, we present $E(\vec{k}_\parallel)$ maps from the pristine reconstructed $Fe_3O_4(001)$ surface and discuss them in terms of final-state scattering (UPD) effects; in Sec. IV B, we show the evolution of the occupied states of this surface with Ni doping; and in Sec. IV C we track systematic changes in unoccupied states of Ni/$Fe_3O_4(001)$ as a function of coverage.

A. Final-state scattering effects in $Fe_3O_4(001)$

The reconstructed surface structure of $Fe_3O_4(001)$ is reflected in reciprocal space, as illustrated in Fig. 1. Figures 1(a) and 1(b) show the corresponding bulk Brillouin zone (BZ) boundaries of an fcc crystal structure in extended zone scheme with a cubic lattice constant $a = 8.44$ Å [56] when the emission angle is tilted towards the [110] and the [010] directions, respectively. Solid and dashed circles represent free-electron final-state wave vectors $\vec{k}_f$, indicating measured points in the bulk BZ in the emission range of E_F and 2 eV below E_F, respectively. Wave vectors $\vec{k}_f$ shown with green (He I_α) and red symbols (He II_α) were calculated as described in the three-step model, where $\vec{k}_\perp$ is not conserved upon transmission through the surface potential step, an effect that is modeled by a refraction of photoelectrons by the potential step at the surface [57]. The magnitudes of $\vec{k}_f$ were determined as $|\vec{k}_f| \approx 0.512\sqrt{E_{\rm kin} + V_0}$, where $E_{\rm kin} = \hbar\omega - E_B - \Phi$ is the kinetic energy of a photoelectron in vacuum after excitation from an initial state with binding energy E_B, Φ is the work function, measured to be 5.22 ±0.19 eV, and the inner potential V_0 was taken as 9.22 eV [18].

Figure 1(c) shows the surface Brillouin zones (SBZ) of the bulk truncated (1 × 1) (blue) and the reconstructed $(\sqrt{2} \times \sqrt{2})$-$R45^\circ$ (red) surface. Note that the high-symmetry points $\overline{M}$ and $\overline{X}$ are also labeled with blue and red according to the respective surface unit cell. The sizes of the bulk and the reconstructed SBZ can be determined with $\overline{\Gamma X}^{\rm bulk} = \sqrt{2}\pi/a$ and $\overline{\Gamma X}^{\rm rec} = \pi/a$, respectively. The LEED image in Fig. 1(d) was taken at 20 eV on the pristine reconstructed $Fe_3O_4(001)$ surface prepared as described in Sec. II. The squares describe the primitive cells in reciprocal space with respect to the reconstructed (red) and bulk truncated (blue) surface. The pattern shows clear evidence for a $(\sqrt{2} \times \sqrt{2})$-$R45^\circ$ reconstruction [20].

The surface electronic structure of $(\sqrt{2}\times\sqrt{2})$-$R45^\circ$ $Fe_3O_4(001)$ was first characterized with angular distribution (θ,ϕ) maps of photoelectrons excited from their fixed initial-state energy E_i, corresponding to $\vec{k}_\parallel$ maps. Figures 1(e) and 1(f) show Fermi-surface maps (FSM, for $E_i = 0$ eV binding energy) taken with He I_α and He II_α excitation, respectively. The squares overlaid refer to SBZ boundaries for bulk-truncated and reconstructed surfaces, as depicted in Fig. 1(c). The magnitude of the parallel momentum is given by $|\vec{k}_\parallel| \approx 0.512\sqrt{E_{\rm kin}}\sin(\theta)$. The influence of surface states on the reconstructed $Fe_3O_4(001)$ was reported to be negligible [18]. Consequently, the observed spectral weight for both He I_α and He II_α photoexcitations originate from the bulk states of electrons populating the t_{2g} band of $Fe^{2+}_{\rm oct}$ ions. The solid lines in Figs. 1(a) and 1(b) trace the final-state wave vectors $\vec{k}_f$. They indicate that He I_α and He II_α photon energies probe different points in the bulk BZ. Interestingly, the He I_α FSM exhibits relatively sharp features of spectral weight that follow the boundaries of the second and third reconstructed SBZ. Notably, the spectral weight is significantly enhanced at the intersection of the high-symmetry points $\overline{X}^{\rm bulk}$ and $\overline{M}^{\rm rec}$ along [110]. This enhancement is particularly pronounced in the He I_α FSM, whereas the He II_α FSM exhibits a weaker spectral weight and cannot resolve the features precisely. These observations suggest that we see some features related to the periodicity of the reconstructed lattice, although no band dispersion near E_F is resolved in the data presented in Sec. IV B. On the other hand, other features do not show any connection to the reciprocal lattice, and they require a different explanation.

It was discovered some time ago that photoelectron diffraction effects in the final state cannot be neglected in such UV excited angular distribution maps of valence states [58]. The RSMS code provides an efficient tool to include such effects (see Sec. III and Ref. [43] for details). In order to elucidate the degree to which final-state scattering is important, Fig. 2 shows the comparison between measured and calculated $E(\vec{k}_\parallel)$ maps for six different fixed energies, for both He I_α [Fig. 2(a)] and He II_α [Fig. 2(c)] excitation. All six energies E_i were measured simultaneously by recording the count rates of six channeltron detectors distributed in the detector plane of the hemispherical energy analyzer [45], using an analyzer pass energy of 5 eV. The first three E_i values (E_F, 0.22 eV, and 0.43 eV) lie within the $Fe^{2+}_{\rm oct}$ $t_{2g}\downarrow$ states, while the last three (1.29, 1.49, and 1.70 eV) are mainly contributed by $Fe^{2+}_{\rm oct}$ $e_g\uparrow$ ($\uparrow$: majority spin) states [see schematic level scheme in Fig. 5(h) and Fe $3d$ surface PDOS calculations in Fig. SI4 [48]]. Therefore, the strong variation between the patterns of the first and the last three E_i can be attributed to the different orbital symmetries and thus to initial-state effects. Within each group only minor changes are observed [Figs. 2(a) and 2(c)], while the corresponding calculated patterns [Figs. 2(b) and 2(d)] show slightly more pronounced changes. We speculate that this might be due to strong electron-phonon scattering effects in the experimental data that lead to broadening [18,22,59] not considered in the LDA + U calculations. Particularly in the outermost parts of the maps, the measurements are in good agreement with the calculations, while the agreement is less good near the center of the patterns.

According to a recent photoemission study [18], no clear evidence for $(\sqrt{2}\times\sqrt{2})$-$R45^\circ$ $Fe_3O_4(001)$ surface could be found in photoemission data. Therefore, we interpret these patterns as emanating from bulk states. The free-electron final-state wave vectors depicted in Figs. 1(a) and 1(b) for He I_α and He II_α excitation illustrate how different bulk states are probed with the two different photon energies. The pronounced difference in the patterns between the two excitations can therefore be attributed to both their initial as well as their final states. Interestingly, the $E(\vec{k}_\parallel)$ maps calculated with the RSMS code for He II_α match the measured patterns very well suggesting that the description of the final state is better at higher energy than at low-photon energy. Indeed, the lower the photoelectron energy, the larger the effect of the potential details on the final-state wave function, including the shape of the surface potential barrier, which is difficult to describe in the muffin-tin approximation.

B. Occupied states of Ni/Fe_3O_4(001)

The $Fe_3O_4(001)$ surface can be functionalized by Ni incorporation by postannealing treatments [26,28,29]. In the ideal case, Ni atoms are expected to occupy one of two subsurface Fe vacancies of the SCV reconstruction. However, with increasing temperature and Ni coverage, Ni-$Fe_{\rm oct}$ substitutional defects can also form. Figures 3(a) and 3(b) show the evolution of Ni $2p_{3/2}$ and Fe $2p_{3/2}$ core-level XP spectra, respectively, taken before and after incorporation of a 26-ML coverage of Ni on $(\sqrt{2}\times\sqrt{2})$-$R45^\circ$ $Fe_3O_4(001)$, where 26-ML coverage is the amount equivalent to 2.3 densely packed layers of Ni, assuming a Ni(001) orientation. The as-grown sample shows three distinct peaks within the Ni $2p_{3/2}$ spectrum, which can be assigned to Ni^0 (852.8 eV) and Ni^{2+} (854.9 eV) charge states and a Ni^{2+}-related satellite peak (861.5 eV) [28]. The relative spectral weight between Ni^0 and Ni^{2+} changes dramatically with postannealing at 607 K. Ni^0 vanishes completely as Ni metal islands on the surface disappear, while the Ni^{2+} signal is greatly enhanced, heralding the incorporation of Ni. The significant apparent increase of the integrated Ni $2p_{3/2}$ signal can be explained with the attenuation within three-dimensional (3D) Ni islands in the as-grown sample [28]. Fe $2p_{3/2}$ core-level XP spectra taken on the pristine sample show a broad peak at ≈711 eV, as a result of multiplet splitting. The spectrum can be deconvoluted into separate multiplets from Fe^{2+} and Fe^{3+} charge states (see Fig. SI3 [48]). The two most dominant spectral contributions are reported to be at energies between 708.3 and 709.3 eV for Fe^{2+}, and between 710.2 and 711.3 eV for Fe^{3+} [60]. The Fe^{3+}/Fe^{2+} ratio is found to be ≈1.9 on the pristine reconstructed $Fe_3O_4(001)$ sample, which is known to be enriched in Fe^{3+} near the surface [20]. It is worth noting that the ratio may be influenced by photoelectron diffraction effects due to the different atomic environments of octahedrally and tetrahedrally coordinated Fe cations. Deposition of 26 ML of Ni reduces the $Fe_3O_4(001)$ surface, and consequently the Fe^{2+} contribution increases in the as-grown sample and the Fe $2p_{3/2}$ peak envelope shifts to lower binding energies. However, the spectral line shape recovers with

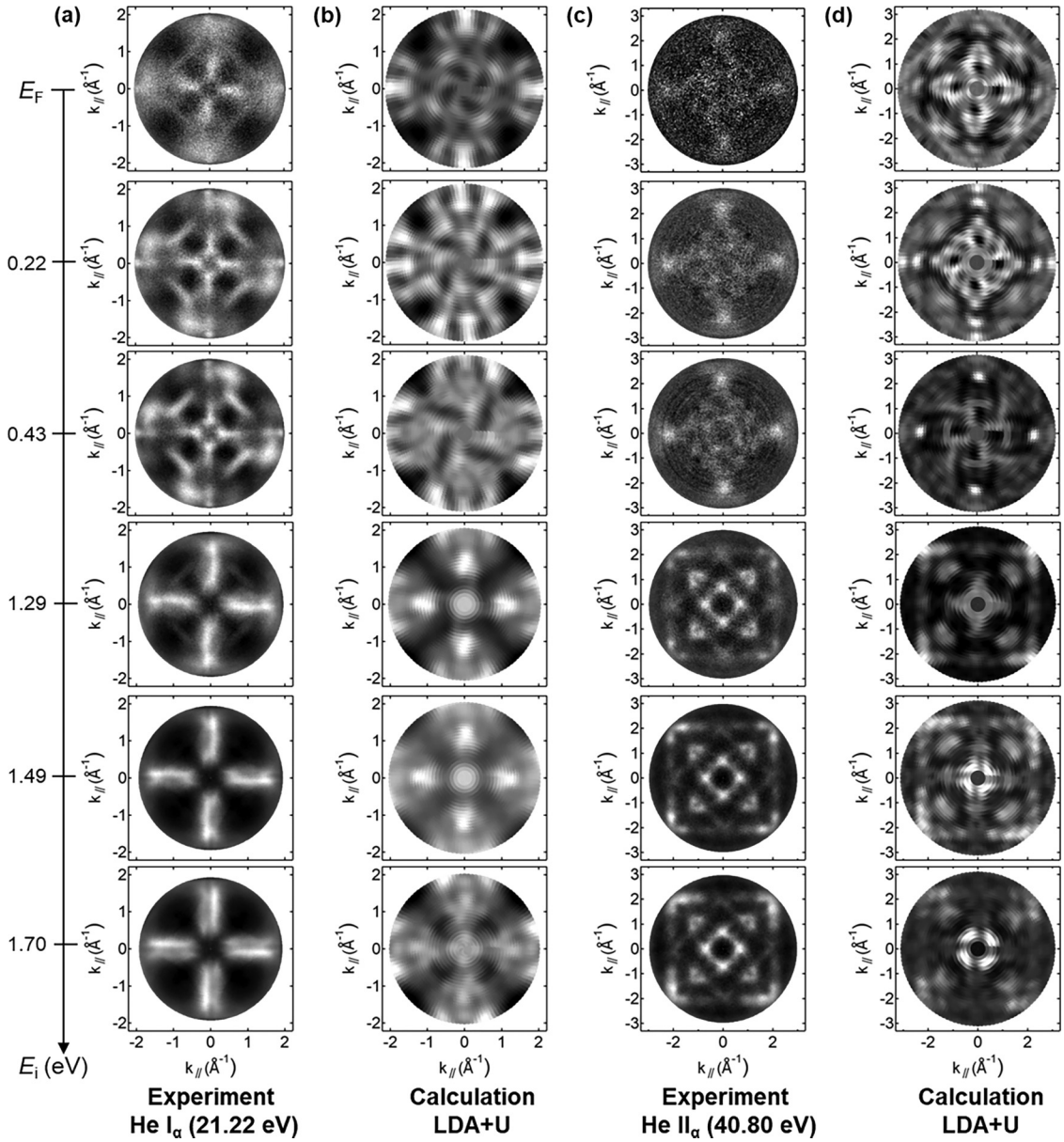

FIG. 2. (a), (c) Angular distribution (θ, ϕ) maps of photoelectrons excited from their fixed initial-state energy E_i and mapped versus $\vec{k}_\parallel$, and (b), (d) the corresponding momentum distributions calculated with the RSMS code for fixed binding energies, highlighting the importance of final-state effects. No symmetry averaging was applied to the experimental patterns. (Top to bottom: E_F, 0.22, 0.43, 1.29, 1.49, and 1.7 eV.)

postannealing, as the Fe^{3+}/Fe^{2+} ratio evolves from ≈1.2 (as-grown) to ≈2.7 (postannealed) (see Fig. SI3 [48]), suggesting that the incorporation of Ni^{2+} into the surface region replaces predominantly Fe^{2+}. When considering the robustness of tetrahedral sites against subsurface cation exchange [29], the Fe $2p_{3/2}$ spectrum must be dominated by Fe^{3+}_{tet} while Ni^{2+} occupies exclusively octahedral sites. To support this argument, the local structure near the surface was investigated with AED measurements performed with Mg K_α excitation of the Ni LMM Auger line [Fig. 3(c)]. The measured pattern shows a fourfold symmetric pattern of mainly forward scattering maxima. In particular, cations on octahedral and tetrahedral sites have different local environments, and they should produce distinctly different emission patterns. Figures 3(d) and 3(e) show simulated diffraction patterns calculated with the EDAC code [55] for emitter atoms placed on octahedral and on tetrahedral sites, respectively. For convenience, Fe emitters were used, but emitting at a kinetic energy of of 840 eV that corresponds roughly to that of the Ni LMM emission. The simulated patterns are a linear combination of individual patterns calculated for Fe emitters in the first several surface layers [Fe_{oct}: (S-0), (S-2), and (S-4), Fe_{tet}: (S-1), (S-3), and (S-5)] (see Fig. SI2 [48]). The comparison between measurement and simulation suggests that incorporated Ni atoms mainly emit from octahedral sites in the lattice, confirming both the experimental results [28,30] and theoretical predictions [29].

ARUPS energy scans were taken with He I$_\alpha$ excitation before and after incorporation of 26 ML of Ni into

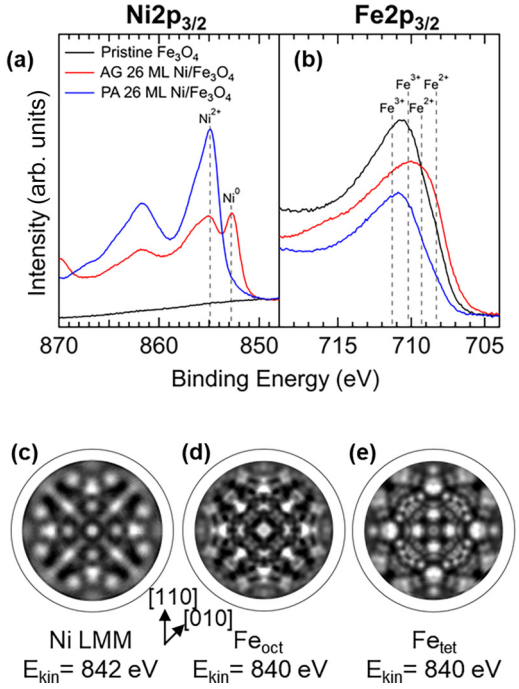

FIG. 3. XP spectra of (a) Ni $2p_{3/2}$ and (b) Fe $2p_{3/2}$ acquired with nonmonochromatized Mg K_α excitation from the pristine sample (black), and from as-grown (AG, red) and postannealed (PA, blue) samples of 26-ML Ni/Fe_3O_4(001). Dashed vertical lines mark main components of individual charge states for Fe $2p_{3/2}$ [60] and Ni $2p_{3/2}$ [28]. (c) Measured Auger electron diffraction pattern of Ni LMM taken after postannealing. EDAC simulations for Fe emission from (d) octahedrally and (e) tetrahedrally coordinated Fe sites calculated with the Ni LMM kinetic energy. The simulated patterns shown here are a linear combination of the patterns individually calculated for the first several layers (see text).

$(\sqrt{2}\times\sqrt{2})$-$R45^\circ$ Fe_3O_4(001) in order to address changes in the occupied electronic states near E_F. Figure 4 shows the measured data before and after the Ni deposition along the high-symmetry directions $\overline{\Gamma M}^{rec}$ ([110]) and $\overline{\Gamma X}^{rec}$ ([010]) of the SBZ of the reconstructed surface, down to 2.6 eV below E_F. The bands in this energy window are examined with momentum and energy distribution curves (MDC and EDC) which are displayed after each curve has been normalized between zero and one to visualize all the features. The high-symmetry points of the reconstructed and bulk SBZ are shown with vertical dashed lines in the MDC plots. When considering the binding energies of the Fe $t_{2g}\downarrow$ of Fe^{2+}_{oct} ions [see Fig. 5(h)], which are located between 0.8 eV binding energy and E_F according to Ref. [18], there is no significant indication of a Fe t_{2g} band dispersion along either direction, as observed in Figs. 4(a) and 4(b). This is likely due to the dominance of broadened quasiparticle states near the Fermi level, as a result of strong electron-lattice coupling [18,22,59]. Such strong correlation effects conceal the information about the delocalization of the $t_{2g}\downarrow$ state due to the broad incoherent states near E_F.

At higher binding energies the scans taken along the [110] azimuth show a band dispersing between two $\overline{M}^{rec}$ points with a band bottom at ≈1.85 eV [see Fig. 4(a)]. The band

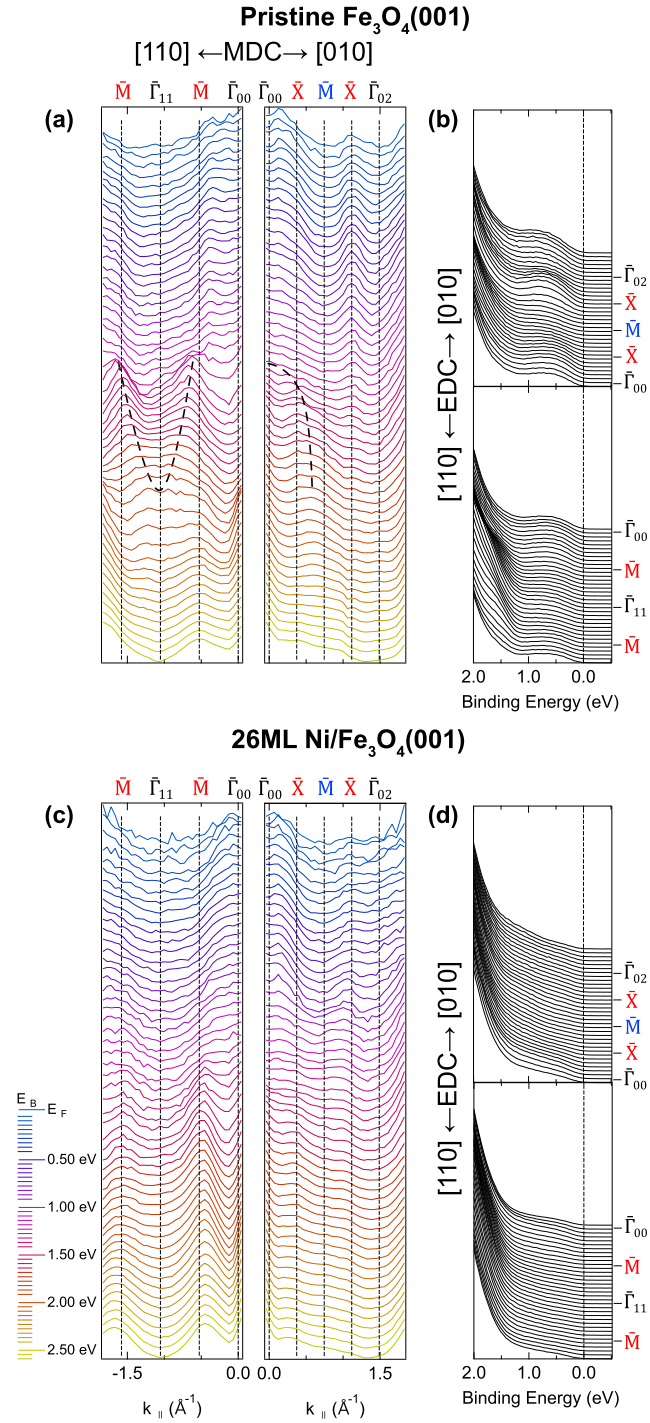

FIG. 4. Half-metal to semiconductor transition of the $(\sqrt{2}\times\sqrt{2})$-$R45^\circ$ Fe_3O_4(001) surface upon Ni doping. (a) MDC and (b) EDC representation of ARUPS energy scans taken along the [110] and [010] directions in the range between E_F and 2.6 eV below E_F. In (b) the energy range is cut to 2.0 eV binding energy in order to highlight the weak emission at low binding energies. The measurements correspond to the $\overline{\Gamma M}$ and $\overline{\Gamma X}$ high-symmetry directions in the SBZ of the reconstructed surface. The dashed lines represent the dispersion of the e_g band from Fe^{2+}_{oct}. (c) MDC and (d) EDC show the analogous data taken after 26 ML of Ni deposition on and incorporation in the reconstructed Fe_3O_4(001) surface. Each curve has been normalized between zero and one to enhance the weak features.

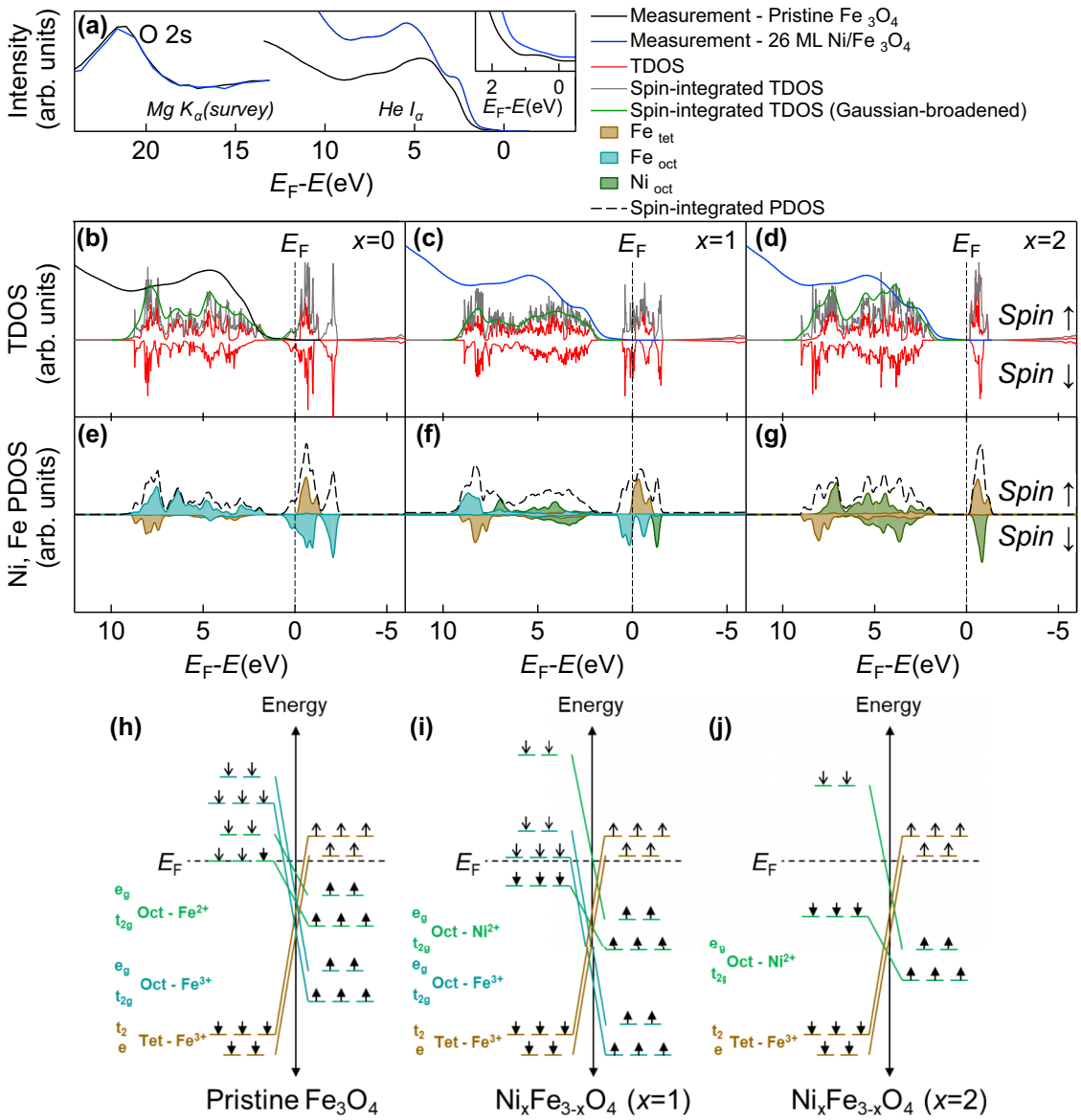

FIG. 5. (a) Comparison of k-space integrated UPS measurements (He I_α) of the valence band region and the O 2s core-level (Mg K_α, extracted from the survey spectra) taken on pristine (black) and postannealed 26-ML $Ni/Fe_3O_4(001)$ (blue). The relative intensity change near E_F after the incorporation is shown in the inset, indicating vanishing electronic states after Ni incorporation. TDOS calculated for $Ni_xFe_{3-x}O_4$ with (b) $x = 0$, (c) $x = 1$, and (d) $x = 2$. Gaussian-broadened (0.5 eV) TDOS for the occupied states given in green curves. (e)–(g) The corresponding projected 3d DOS of Fe_{oct} (cyan), Fe_{tet}(brown), and Ni_{oct} (green) (Gaussian broadening: 0.2 eV). (h), (i) Schematic representation of crystal field ground-state spin configurations of $Ni_xFe_{3-x}O_4$ for (h) $x = 0$, (i) $x = 1$, and (j) $x = 2$ based on the calculations in (e)–(g). Energy intervals are not to scale.

dispersion is visible in its corresponding EDC representation [see Fig. 4(b) and zoomed-in version for a better visibility in Fig. SI9 [48]]. Note that the high-symmetry $\overline{M}^{rec}$ points superimpose with $\overline{X}^{bulk}$. The position of this band and its dispersion suggest that $e_g \uparrow$ states of Fe^{2+}_{oct} ions are delocalized (see Fig. SI9 [48]). This same state is also observed along the [010] direction with downward dispersion between $\overline{\Gamma}_{00}$ and $\overline{M}^{bulk}$. Along this direction, an additional feature is observed near E_F centered at $\overline{X}$ point. Recalling Figs. 1(c) and 1(e), this emission appears to be connected with the boundaries of the second SBZ of the reconstructed surface. This feature is present over the entire occupied bandwidth of the $t_{2g} \downarrow$ band without noticeable dispersion. Overall, the dispersion observed in our data reproduces qualitatively the results of Ref. [18].

The MDC plots taken after Ni incorporation [Fig. 4(c)] show that the dispersion of the $e_g \uparrow$ band of Fe^{2+}_{oct} is reduced, and that the emission near E_F at $\overline{X}$ is much less prominent and shows some slight dispersion. The vertical dashed lines, which refer to high-symmetry points of the reconstructed SBZ, are left the same for comparison, although the incorporation of Ni into the lattice transforms the $(\sqrt{2} \times \sqrt{2})$-$R45^\circ$ reconstruction

into a (1×1) structure, as observed by LEED (see Fig. SI7 [48]). The change in the band structure is more pronounced in the EDC plot of Fig. 4(d), showing that the 26-ML Ni incorporation significantly suppresses the spectral weight just below E_F.

Fixed energy maps acquired on the pristine reconstructed surface, the as-grown 26-ML Ni/Fe_3O_4(001) as well as the postannealed sample are given in Figs. SI5 and SI6 for a complete overview in momentum space [48]. From these data it becomes more obvious that the changes in the $t_{2g} \downarrow$ state at binding energies below 0.8 eV are more dramatic than the changes in the $e_g \uparrow$ band at higher binding energies. The feature near E_F following the boundary of the reconstructed SBZ has vanished, mirroring the disappearance of the LEED spots due to the lifting of the $(\sqrt{2} \times \sqrt{2})$-$R45^\circ$ reconstruction (see Fig. SI7 [48]).

For comparison with DOS calculations, all EDC curves along the two high-symmetry directions were combined to yield the angle-integrated DOS shown in Fig. 5(a). The UPS measurements are given together with XPS measurements of the O 2*s* shallow core level, showing a nearly identical binding energy of 21.4 eV before and after Ni incorporation. The angle-integrated UPS spectra of the pristine sample and the postannealed 26-ML Ni-doped sample are compared to the calculated total density of state (TDOS) and bulk Fe and Ni 3*d* partial densities of state (PDOS) in $Ni_xFe_{3-x}O_4$ for $x = 0$, $x = 1$, and $x = 2$ [see Figs. 5(b)–5(g)]. A hypothetical nickel ferritelike structure for $x = 2$ was considered in our qualitative comparison because quantitative XPS suggested a considerable excess of Ni within the probing depth [28]. Figures 5(b) and 5(e) represent the half-metallic DOS of the Fe_3O_4 valence band, as reproduced with the parameters given by Ref. [20]. The results of the calculations agree with the measurements, particularly for the deeper lying Fe^{3+}_{oct} states near 4 eV and the Fe^{3+}_{tet} states near 8 eV, as well as for the $t_{2g} \downarrow$ state near E_F [see inset in Fig. 5(a)].

The UPS spectrum of the 26-ML Ni-incorporated Fe_3O_4 is compared to the calculations performed for $x = 1$ and $x = 2$ in a search for the best match between the two. Based on the XPS measurements, all the incorporated Ni atoms were assumed to be in the Ni^{2+} oxidation state. The calculations were performed for bulk systems, while experimentally the $Ni_xFe_{3-x}O_4$ phase is a thin layer whose Fermi energy alignment with the Fe_3O_4 substrate is a subtle issue. Experimentally, we found that the O 2*s* core level does not shift upon Ni incorporation. Therefore, we have aligned the energy scale of $Ni_xFe_{3-x}O_4$ DOS calculations in Fig. 5 such as the O 2*s* peak coincides with that of Fe_3O_4 (see also Fig. SI8 for the extended TDOS calculations down to the O 2*s* core level [48]). This procedure for locating the position of E_F in the calculated DOS appears justified because the O 2*s* level does not shift upon the incorporation of 26 ML of Ni, as demonstrated in Fig. 5(a). Figures 5(b)–5(g) represent the TDOS and Ni,Fe 3*d* PDOS after the O 2*s* core level has been aligned with that of $x = 0$. For $x = 1$ this energy alignment moves the Fermi level into the conduction band [see Figs. 5(c) and 5(f)], which is in contrast with the known semiconducting properties of Ni ferrite [39–42]. This problem is likely to be due to the LDA + U calculation, which underestimates the size of the band gap by at least 0.6 eV. For $x = 2$, the issue is more complex. Here the resulting DOS structure shows that E_F lies in the band gap [see Figs. 5(d) and 5(g)]. Assuming a charge state of 2+ for all Ni cations on octahedral sites, electron counting leads to an extra hole charge per formula unit. This is reflected in the LDA + U calculation for $x = 2$ before the O 2*s* energy alignment (see Fig. SI9c [48]) where E_F is located below the top of the valence band. However, as the system consists of layered structures comprising the Fe_3O_4 bulk and overlayers of Ni_2FeO_4 and/or $NiFe_2O_4$, with a Ni concentration gradient, the respective Fermi level of the bulk compound becomes irrelevant. It suggests that hole doping of the $x = 2$ surface layer seems to be a more appropriate picture of the system.

When comparing the angle-integrated UPS spectra of the postannealed 26-ML Ni-doped sample to the $x = 1$ and $x = 2$ calculations, a slightly better match is observed for $x = 2$ than $x = 1$. Particularly, the measured broad peak near 5.5 eV is in good agreement with the TDOS calculation, and the PDOS calculations suggest that this state originates from the Ni_{oct} sites. It is also worth noting that states near 8 eV, dominated by the Fe_{tet} atoms, remain robust upon the 26-ML Ni incorporation, which is consistent with the findings from the XPD measurements [28].

According to Hund's rule, the lowest Coulomb energy favors the high-spin state being the ground-state spin configuration, as any spin flip transforms the electronic structure to an excited spin state with an energy cost $3J$ [61]. As shown in the schemes of Figs. 5(h)–5(j), the two extra electrons of Ni^{2+} fill the $t_{2g} \downarrow$ band in the ground state. This results in the reduction in DOS at E_F, evidenced by the opening band gap, i.e., a half-metal to a semiconductor transition. However, the measured spectral weight near E_F has not completely vanished with Ni incorporation. This could indicate the presence of remaining metallic states due to gradients in the Ni concentration with depth. After postannealing, the 26-ML Ni on Fe_3O_4(001) sample is in a metastable $Ni_xFe_{3-x}O_4$(001) composition with $x \approx 2$ within the probing depth of XPS [28]. Such a ferritelike structure can form when excess Ni ions beyond $x > 1$ stay in the Ni^{2+} chemical state and substitute Fe^{3+}_{oct} cations according to XPS measurements shown in Fig. 3. In this state, the charge neutrality cannot be maintained, and an extra hole charge leads to a metallic conduction band [see raw PDOS calculation for hypothetical $Ni_xFe_{3-x}O_4$(001) for $x = 2$ in Fig. SI9 [48]]. Therefore, the weak emission near E_F observed in the ARUPS energy scans of Fig. 4(d) may be linked to the Ni oversaturation. Strong correlation effects might still remain after Ni incorporation, and some minor occupation of tetrahedral sites by Ni ions, observed on nickel-ferrite nanocrystalline structures [62], cannot be excluded with our AED data.

C. Unoccupied states of Ni/Fe_3O_4(001)

In this study we employed x-ray absorption near-edge structure (XANES) measurements in Auger electron yield (AEY) mode to investigate the evolution of unoccupied Fe and Ni 3*d* states upon deposition of Ni on Fe_3O_4(001) with varying coverages. By detecting Ni LMM and Fe LMM intensities, the measurements are not influenced by secondary electrons,

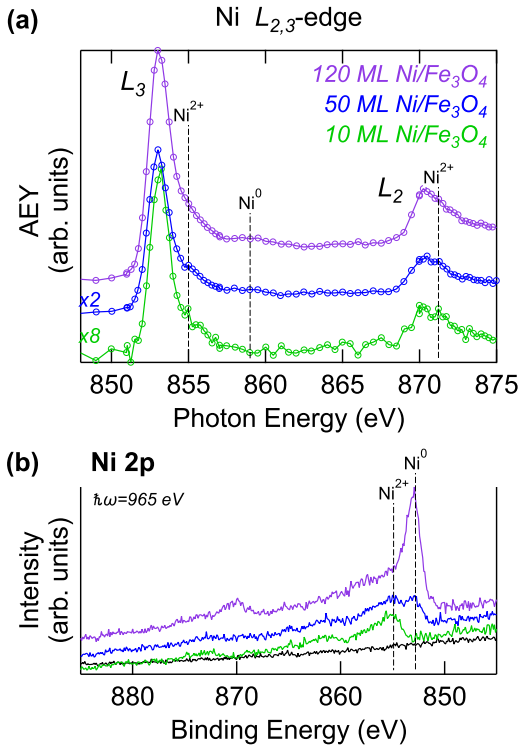

FIG. 6. (a) Ni $L_{2,3}$ edge measured in AEY mode taken after deposition of 10 ML (green), 50 ML (blue), and 120 ML (purple) of Ni on Fe_3O_4(001) at 607 K. A scaling parameter was applied to each spectrum by aligning them to equal peak height to highlight the relative changes, and the spectra shown here were scaled with a multiplier for comparison. Metallic and $NiFe_2O_4$ specific Ni^0 and Ni^{2+} peak positions are represented by dashed lines. (b) Corresponding XP spectra taken with a photon energy $\hbar\omega = 965$ eV. Vertical dashed lines indicate the literature values oxidation states Ni^0 and Ni^{2+} [28].

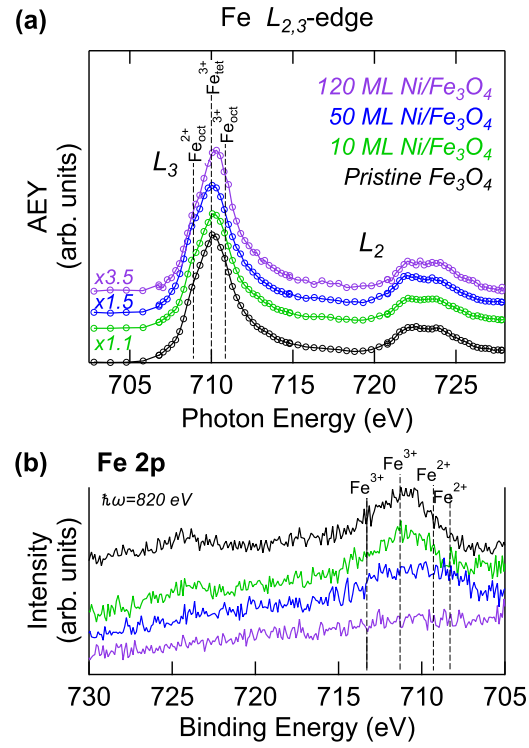

FIG. 7. (a) Fe $L_{2,3}$ edge measured in AEY mode taken on the pristine sample (black), after deposition of 10 ML (green), 50 ML (blue), and 120 ML (purple) of Ni on Fe_3O_4(001) at 607 K. A scaling parameter was applied to each spectrum by aligning them to equal peak height to highlight the relative changes, and the spectra shown here were scaled with a multiplier for comparison. Vertical dashed lines indicate the absorption energy for the each inequivalent Fe cation in the sublattice [63]. (b) Corresponding XP spectra taken with a photon energy $\hbar\omega = 820$ eV. Vertical dashed lines indicate the positions of the two most dominating divalent and trivalent multiplet components.

leading to increased surface sensitivity. Figures 6(a) and 7(a) show $L_{2,3}$ XANES measurements of Ni and Fe, respectively, acquired on the pristine sample and after 10, 50, and 120 ML of Ni, deposited at 607 K. Note that no postannealing was applied in these experiments, but the deposition at high sample temperature led to Ni incorporation already during the deposition. Additionally, Fe $2p$ and Ni $2p$ core-level XP spectra measured at normal emission before and after each deposition are shown in Figs. 6(b) and 7(b). The photon energy is tuned for both Fe $2p_{3/2}$ and Ni $2p_{3/2}$ regions to extract the photoelectrons at a kinetic energy of ≈ 110 eV to maximize the surface sensitivity for the XPS measurements.

In Fig. 6(b), two distinct peaks are observed at 854.9 and 861.4 eV in the Ni $2p$ region after 10 ML of Ni deposition, which are assigned to the Ni $2p_{3/2}$ main line of Ni^{2+} ions and the corresponding satellite characteristic of $NiFe_2O_4$ [64], respectively. Incorporating Ni into the magnetite lattice is a slow process; any excess Ni accumulates on the surface in the form of metallic Ni clusters [28]. Therefore, when the coverage is increased to 50 ML, an additional peak emerges at 852.8 eV, representing the Ni^0 chemical state. At 120-ML Ni coverage, all the signal related to incorporated Ni atoms, i.e., Ni^{2+}, is attenuated by the metallic clusters, resulting in one dominant peak at the Ni^0 binding energy. Due to the existence of a metallic Ni overlayer, the XPS probing depth for the substrate becomes reduced. Consequently, the Ni^{2+} XPS signal obtained from the 50- and 120-ML depositions has lower spectral intensity. Based on the incorporation kinetics and growth durations [28], the 50- and 120-ML depositions are expected to be oversaturated ($x > 1$). These findings are consistent with the data set taken with the laboratory source shown in Fig. 3(a).

Figure 6(a) shows a peak at 853 eV at the Ni L_3 edge for the 10-, 50-, and 120-ML Ni/Fe_3O_4(001) samples, indicative of a $NiFe_2O_4$ related Ni^{2+}, with a broad shoulder at $\approx$2 eV higher energy contributing to the line shape. These peaks originate from a transition from the Ni $2p$ core level to unoccupied $3d$ states, and they show $2p^5_{3/2}3d^9$ final-state character [37,65]. Particularly, the 10-ML sample matches a previous study by van der Laan *et al.* [37], where a XANES simulation for $NiFe_2O_4$ with Ni occupying octahedral sites is shown to reproduce the measurement, including the two-peak structure of the L_2 edge. With increasing coverage, the visibility of the Ni^{2+} component in the Ni L_2 edge decreases, as the intensity of Ni^0 from the metallic clusters increases. The presence of

metallic Ni clusters at higher coverages also manifests itself in a broadening of the Ni L_2 edge and a weak broad peak around 859 eV [65]. The Ni $L_{2,3}$-edge XANES measurements are thus consistent with the XPS observations.

The Fe L_3 edge of pristine reconstructed $Fe_3O_4(001)$ shows a broad peak as a result of three inequivalent sublattices of Fe cations and a multiplet splitting that occurs due to the open $3d$ shell [Fig. 7(a)]. The shoulders at the low- and high-energy sides are mainly contributed by $Fe^{2+}O_6$ and $Fe^{3+}O_6$ octahedra, respectively. They sandwich the signal from $Fe^{3+}O_4$ tetrahedra [50,63,65,66]. The energy separation between $Fe^{3+}O_6$ and $Fe^{2+}O_6$ is approximately 2.08 eV, and that between $Fe^{3+}O_6$ and $Fe^{3+}O_4$ is about 1 eV [61]. Concomitant with the attenuation of the Ni^{2+} signal in XPS [Fig. 6(b)], the absorption intensity of the Fe $L_{2,3}$ edges drops significantly as the Ni coverage is increased [note the multipliers on the left-hand side of the normalized spectra in Fig. 7(a)]. This is due to both Ni-Fe cation exchange in the octahedral sublattice and the presence of metallic Ni clusters on the surface. For 10-ML Ni coverage, the former argument dominates the spectral changes (see the raw data in Fig. SI11 [48]). The stronger attenuation of the Fe $L_{2,3}$ edges after Ni coverages of 50 and 120 ML is due to both factors when considering the Ni^0 accumulation on the surface. The presence of metallic Ni islands on the surface should not influence the spectral shape of the Fe $L_{2,3}$ edges nor that of the O K edge.

To obtain a complete picture of the incorporation process, the O K edge was also measured before and after Ni deposition. Figure 8(a) shows O K-edge XANES data which reflect the evolution of unoccupied $3d$ and $4sp$ cation states hybridized with O $2p$ states as a function of Ni coverage. Considering that all the oxidized species are Ni and Fe related, the spectral area under the curves can be normalized with a multiplier to the pristine Fe_3O_4 spectrum in order to trace the relative changes. For the pristine sample, the Fe $3d$ related absorption spectrum exhibits two distinct peaks at lower energy associated with t_{2g} and e_g states, followed by a Fe $4sp$ related absorption with two broad peaks at higher energies [51,67]. With increasing Ni coverage, $Fe^{2+}O_6$ to $Ni^{2+}O_6$ exchange reduces the t_{2g} related absorption as two extra electrons of Ni^{2+} fill the $t_{2g}\downarrow$ band completely. The remaining $3d$ related peaks slightly shift to higher energy and can be correlated to increasing contributions of unoccupied $e\uparrow$ and $t_2\uparrow$ states. The reduction in t_{2g} and e_g absorption due to Fe-Ni exchange in octahedral sites further produces a systematic rise in the spectral weight at ≈531.4 eV. The position of O $2p$ hybridized with t_{2g} states fades away with increasing Ni density, while a hybridized state appears in the valley between $3d$ and $4sp$ absorption, which is attributed to the e_g band of the Ni^{2+} [see Figs. 5(i) and 5(j)]. Considering the difference in crystal field splitting strength between Fe_{oct} (0.6 eV [50]) and Ni_{oct} (1.2 eV [37]), a shift of the e_g absorption to higher energy is expected. Moreover, the cation exchange in the sublattice of octahedral sites also significantly influences the $4sp$ hybridization levels, as the absorption intensity is reduced at 540.5 eV while it increases at 539.1 eV. Along with the XPD results shown in Fig. 3, the redistribution of absorption intensities can be correlated to the replacement of Fe_{oct} with Ni_{oct}. The spectral difference between the pristine sample and 10-ML points to the presence of Ni^{2+}_{oct} hybridized states at 532.1, 535.6, and 539.5 eV originating from $x \approx 1$ in $Ni_xFe_{3-x}O_4(001)$. When the composition is $x > 1$ in $Ni_xFe_{3-x}O_4(001)$, the intensities at 532.1, 534.1, and 539.1 eV become more prominent, as seen in the 50- and 120-ML samples relative to the 10-ML sample, while the intensities at 529.1 and 540.3 eV decrease. These latter states can be attributed to the hybridized states of the Fe^{3+}_{oct} atoms that are replaced in the oversaturated case.

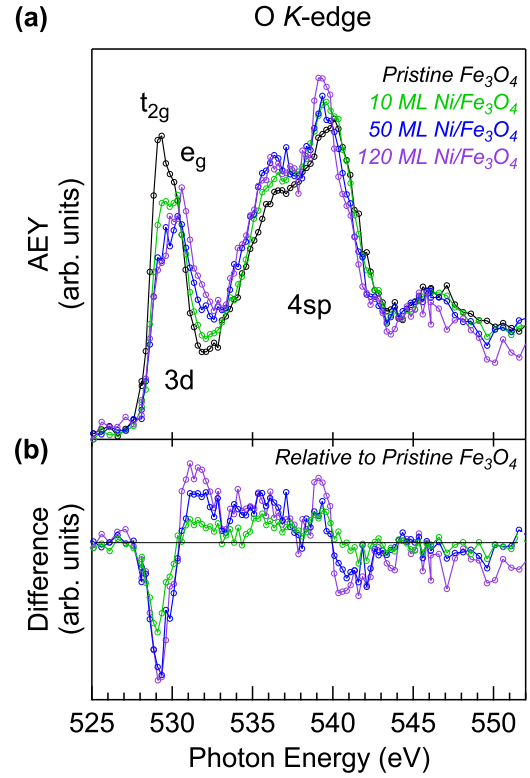

FIG. 8. (a) O K edge measured in AEY mode taken on the pristine sample (black), after deposition of 10 ML (green), 50 ML (blue), and 120 ML (purple) of Ni on $Fe_3O_4(001)$. The features related to O $2p$ hybridization with $3d$ and $4sp$ cation states are indicated. For comparison, the spectral area under the curves was normalized to that of a pristine sample. (b) The difference spectra show the relative changes compared to the spectrum of the pristine sample.

V. CONCLUSION

To gain a more complete understanding of the electronic structure of the $Ni/Fe_3O_4(001)$ surfaces, we first investigated the occupied states of pristine magnetite. We examined partially filled t_{2g} and deeper e_g levels using ARPES measurements and analyzed the data with the RSMS code. Alternatively, we observed that final-state effects are prominent in photoemission angular distribution maps from valence levels. The RSMS simulations, which include photoelectron diffraction effects, show a good match with the measured data. In particular, excellent agreement was achieved for He II_α excitation suggesting an accurate description of the initial and final states.

The incorporation of 26-ML Ni in $Fe_3O_4(001)$ results in the occupation of Ni atoms mainly in octahedral coordination, leading to the lifting of the surface reconstruction.

ARUPS measurements show that the states near E_F disappear almost completely upon Ni incorporation, providing direct experimental evidence of a band-gap opening. Remaining weak emission near E_F was discussed in terms of compositional gradients near the surface. To further understand the composition of $Ni_xFe_{3-x}O_4$, obtained after the incorporation of 26-ML $Ni/Fe_3O_4(001)$, the angle-integrated UPS spectra were compared to TDOS and PDOS calculations performed with LDA + U for $x = 1$ and $x = 2$, with the latter showing a slightly better match. Based on the agreement between experimental and computational results presented in this study, and in combination with our previous study where we explored the structural properties of $Ni_xFe_{3-x}O_4$ (for $x = 2$) [28], a more complete picture of a Ni_2FeO_4-like compound is achieved.

Moreover, the unoccupied electronic states of $Ni_xFe_{3-x}O_4$ were measured for $x \approx 1$ (10 ML) and $x > 1$ (50 and 120 ML). The Ni $L_{2,3}$-edge spectra were successfully reproduced for $NiFe_2O_4$, reflecting the changes upon Ni incorporation. The Fe L_3 edge shifts to higher photon energy, where Fe^{3+}_{oct} and Fe^{3+}_{tet} were previously reported in the literature, as a function of incorporated Ni. These findings are consistent with the XPS and XPD analyses. The systematic changes as a function of Ni coverage observed in the O K edge confirm the filling of the $t_{2g} \downarrow$ band and unravel the emergence and shifting of new hybrid states at higher energy, attributed mainly to Fe^{2+}_{oct}-Ni^{2+}_{oct} exchanges upon Ni incorporation. These hybridized states can be tuned by the amount of incorporated Ni atoms. These states might be responsible for the enhanced catalytic activity of the $x \geqslant 1$ surface [26]. Therefore, we believe that our experimental results on the electronic structure of the $Ni/Fe_3O_4(001)$ model system may provide useful information for enhancing the efficiency of NiFe-based (photo)electrodes in electrochemical and photocatalytic water oxidation.

All data used to produce the findings of this paper are publicly available on the Zenodo repository [68].

ACKNOWLEDGMENTS

This project has been funded under the University Research Priority Program, Light to Chemical Energy Conversion (URPP-LightChEC), of the University of Zurich. The work presented in Sec. IV C was performed at the In Situ Spectroscopy (X07DB) beamline of the Swiss Light Source, Paul Scherrer Institut, Villigen-PSI, Switzerland using the SLIC chamber [49]. J.T.D. acknowledges funding from European Union's Horizon 2020 under MCSA Grant No. 801459, FP-RESOMUS. The authors thank Prof. T. Greber for fruitful discussions.

[1] Z. Zhang and S. Satpathy, Electron states, magnetism, and the Verwey transition in magnetite, Phys. Rev. B **44**, 13319 (1991).
[2] A. Yanase and N. Hamada, Electronic structure in high temperature phase of Fe_3O_4, J. Phys. Soc. Jpn. **68**, 1607 (1999).
[3] A. Yanase and K. Siratori, Band structure in the high temperature phase of Fe_3O_4, J. Phys. Soc. Jpn. **53**, 312 (1984).
[4] S. Morton, G. D. Waddill, S. Kim, I. K. Schuller, S. A. Chambers, and J. G. Tobin, Spin-resolved photoelectron spectroscopy of Fe_3O_4, Surf. Sci. **513**, L451 (2002).
[5] C. Felser, G. H. Fecher, and B. Balke, Spintronics: A challenge for materials science and solid-state chemistry, Angew. Chem., Int. Ed. **46**, 668 (2007).
[6] E. J. Verwey and P. W. Haayman, Electronic conductivity and transition point of magnetite ("Fe_3O_4"), Physica (Amsterdam) **8**, 979 (1941).
[7] J. Yoshida and S. Iida, X-ray diffraction study on the low temperature phase of magnetite, J. Phys. Soc. Jpn. **42**, 230 (1977).
[8] M. S. Senn, J. P. Wright, and J. P. Attfield, Charge order and three-site distortions in the Verwey structure of magnetite, Nature (London) **481**, 173 (2012).
[9] H. P. Pinto and S. D. Elliott, Mechanism of the Verwey transition in magnetite: Jahn-Teller distortion and charge ordering patterns, J. Phys.: Condens. Matter **18**, 10427 (2006).
[10] P. Piekarz, K. Parlinski, and A. M. Oleś, Mechanism of the Verwey transition in magnetite, Phys. Rev. Lett. **97**, 156402 (2006).
[11] E. J. Verwey, P. W. Haayman, and F. C. Romeijn, Physical properties and cation arrangement of oxides with spinel structures II. Electronic conductivity, J. Chem. Phys. **15**, 181 (1947).
[12] C. Wei, Z. Feng, G. G. Scherer, J. Barber, Y. Shao-Horn, and Z. J. Xu, Cations in octahedral sites: A descriptor for oxygen electrocatalysis on transition-metal spinels, Adv. Mater. **29**, 1606800 (2017).
[13] X. Xie, L. Du, L. Yan, S. Park, Y. Qiu, J. Sokolowski, W. Wang, and Y. Shao, Oxygen evolution reaction in alkaline environment: Material challenges and solutions, Adv. Funct. Mater. **32**, 2110036 (2022).
[14] H. Magnan, P. Le Fèvre, D. Chandesris, P. Krüger, S. Bourgeois, B. Domenichini, A. Verdini, L. Floreano, and A. Morgante, Resonant photoelectron and photoelectron diffraction across the Fe L_3 edge of Fe_3O_4, Phys. Rev. B **81**, 085121 (2010).
[15] J. Chen, D. J. Huang, A. Tanaka, C. F. Chang, S. C. Chung, W. B. Wu, and C. T. Chen, Magnetic circular dichroism in Fe 2p resonant photoemission of magnetite, Phys. Rev. B **69**, 085107 (2004).
[16] J. G. Tobin, S. A. Morton, S. W. Yu, G. D. Waddill, I. K. Schuller, and S. A. Chambers, Spin resolved photoelectron spectroscopy of Fe_3O_4: the case against half-metallicity, J. Phys.: Condens. Matter **19**, 315218 (2007).
[17] M. Fonin, R. Pentcheva, Y. S. Dedkov, M. Sperlich, D. V. Vyalikh, M. Scheffler, U. Rüdiger, and G. Güntherodt, Surface electronic structure of the $Fe_3O_4(100)$: Evidence of a half-metal to metal transition, Phys. Rev. B **72**, 104436 (2005).
[18] W. Wang, J.-M. Mariot, M. C. Richter, O. Heckmann, W. Ndiaye, P. De Padova, A. Taleb-Ibrahimi, P. Le Fèvre, F. Bertran, F. Bondino, E. Magnano, J. Krempaský, P. Blaha, C. Cacho, F. Parmigiani, and K. Hricovini, Fe t_{2g} band dispersion and spin polarization in thin films of $Fe_3O_4(001)/MgO(001)$: Half-metallicity of magnetite revisited, Phys. Rev. B **87**, 085118 (2013).
[19] F.-Y. Ran, Y. Tsunemaru, T. Hasegawa, Y. Takeichi, A. Harasawa, K. Yaji, S. Kim, and A. Kakizaki, Angle-resolved

photoemission study of Fe_3O_4(001) films across Verwey transition, J. Phys. D: Appl. Phys. **45**, 275002 (2012).

[20] R. Bliem, E. McDermott, P. Ferstl, M. Setvin, O. Gamba, J. Pavelec, M. A. Schneider, M. Schmid, U. Diebold, P. Blaha, L. Hammer, and G. S. Parkinson, Subsurface cation vacancy stabilization of the magnetite (001) surface, Science **346**, 1215 (2014).

[21] J. Chen, C. F. Chang, W. P. Wu, A. D. Rata, T. Hibma, S. C. Chung, S.-G. Shyu, C.-C. Wu, and C. T. Chen, Electron correlation effects in half-metallic transition metal oxides, Surf. Rev. Lett. **09**, 1007 (2002).

[22] D. Ihle and B. Lorenz, Small-polaron conduction and short-range order in Fe_3O_4, J. Phys. C: Solid State Phys. **19**, 5239 (1986).

[23] M. Taguchi, A. Chainani, S. Ueda, M. Matsunami, Y. Ishida, R. Eguchi, S. Tsuda, Y. Takata, M. Yabashi, K. Tamasaku, Y. Nishino, T. Ishikawa, H. Daimon, S. Todo, H. Tanaka, M. Oura, Y. Senba, H. Ohashi, and S. Shin, Temperature dependence of magnetically active charge excitations in magnetite across the Verwey transition, Phys. Rev. Lett. **115**, 256405 (2015).

[24] E. Baldini, C. A. Belvin, M. Rodriguez-Vega, I. O. Ozel, D. Legut, A. Kozłowski, A. M. Oleś, K. Parlinski, P. Piekarz, J. Lorenzana, G. A. Fiete, and N. Gedik, Discovery of the soft electronic modes of the trimeron order in magnetite, Nat. Phys. **16**, 541 (2020).

[25] D. Hong, Y. Yamada, T. Nagatomi, Y. Takai, and S. Fukuzumi, Catalysis of nickel ferrite for photocatalytic water oxidation using $[Ru(bpy)_3]^{2+}$ and $S_2O_8^{2-}$, J. Am. Chem. Soc. **134**, 19572 (2012).

[26] F. Mirabella, M. Müllner, T. Touzalin, M. Riva, Z. Jakub, F. Kraushofer, M. Schmid, M. T. Koper, G. S. Parkinson, and U. Diebold, Ni-modified Fe_3O_4(001) surface as a simple model system for understanding the oxygen evolution reaction, Electrochim. Acta **389**, 138638 (2021).

[27] D. H. Taffa, R. Dillert, A. C. Ulpe, K. C. L. Bauerfeind, T. Bredow, D. W. Bahnemann, and M. Wark, Photoelectrochemical and theoretical investigations of spinel type ferrites ($M_xFe_{3-x}O_4$) for water splitting: A mini-review, J. Photon. Energy **7**, 012009 (2017).

[28] M. Taskin, Z. Novotny, M. Hengsberger, and J. Osterwalder, Formation of $Ni_xFe_{3-x}O_4$ on Fe_3O_4(001), Phys. Rev. Mater. **7**, 055801 (2023).

[29] R. Bliem, J. Pavelec, O. Gamba, E. McDermott, Z. Wang, S. Gerhold, M. Wagner, J. Osiecki, K. Schulte, M. Schmid, P. Blaha, U. Diebold, and G. S. Parkinson, Adsorption and incorporation of transition metals at the magnetite Fe_3O_4(001) surface, Phys. Rev. B **92**, 075440 (2015).

[30] P. T. Ryan, Z. Jakub, J. Balajka, J. Hulva, M. Meier, J. T. Küchle, P. J. Blowey, P. K. Thakur, C. Franchini, D. J. Payne, D. P. Woodruff, L. A. Rochford, F. Allegretti, T. L. Lee, G. S. Parkinson, and D. A. Duncan, Direct measurement of Ni incorporation into Fe_3O_4(001), Phys. Chem. Chem. Phys. **20**, 16469 (2018).

[31] G. S. Parkinson, Iron oxide surfaces, Surf. Sci. Rep. **71**, 272 (2016).

[32] Z. Jakub, J. Hulva, F. Mirabella, F. Kraushofer, M. Meier, R. Bliem, U. Diebold, and G. S. Parkinson, Nickel doping enhances the reactivity of Fe_3O_4(001) to water, J. Phys. Chem. C **123**, 15038 (2019).

[33] X. Shi, Y.-F. Li, S. L. Bernasek, and A. Selloni, Structure of the $NiFe_2O_4$(001) surface in contact with gaseous O_2 and water vapor, Surf. Sci. **640**, 73 (2015).

[34] M. Naveed-Ul-Haq and S. Hussain, Pressure-induced structural, electronic, and magnetic evolution in cubic inverse spinel $NiFe_2O_4$, an *ab-initio* study, Appl. Phys. A **128**, 30 (2022).

[35] Q. C. Sun, H. Sims, D. Mazumdar, J. X. Ma, B. S. Holinsworth, K. R. O'Neal, G. Kim, W. H. Butler, A. Gupta, and J. L. Musfeldt, Optical band gap hierarchy in a magnetic oxide: Electronic structure of $NiFe_2O_4$, Phys. Rev. B **86**, 205106 (2012).

[36] B. S. Holinsworth, H. Sims, J. G. Cherian, D. Mazumdar, N. C. Harms, B. C. L. Chapman, A. Gupta, S. A. McGill, and J. L. Musfeldt, Magnetic field tunability of spin-polarized excitations in a high-temperature magnet, Phys. Rev. B **96**, 094427 (2017).

[37] G. van der Laan, C. M. B. Henderson, R. A. D. Pattrick, S. S. Dhesi, P. F. Schofield, E. Dudzik, and D. J. Vaughan, Orbital polarization in $NiFe_2O_4$ measured by Ni-2*p* x-ray magnetic circular dichroism, Phys. Rev. B **59**, 4314 (1999).

[38] C. Klewe, M. Meinert, A. Boehnke, K. Kuepper, E. Arenholz, A. Gupta, J. M. Schmalhorst, T. Kuschel, and G. Reiss, Physical characteristics and cation distribution of $NiFe_2O_4$ thin films with high resistivity prepared by reactive co-sputtering, J. Appl. Phys. **115**, 123903 (2014).

[39] R. D. Waldron, Infrared spectra of ferrites, Phys. Rev. **99**, 1727 (1955).

[40] S. Balaji, R. Kalai Selvan, L. John Berchmans, S. Angappan, K. Subramanian, and C. Augustin, Combustion synthesis and characterization of Sn^{4+} substituted nanocrystalline $NiFe_2O_4$, Mater. Sci. Eng.: B **119**, 119 (2005).

[41] J. Haetge, C. Suchomski, and T. Brezesinski, Ordered mesoporous MFe_2O_4 (M = Co, Cu, Mg, Ni, Zn) thin films with nanocrystalline walls, uniform 16 nm diameter pores and high thermal stability: Template-directed synthesis and characterization of redox active trevorite, Inorg. Chem. **49**, 11619 (2010).

[42] R. C. Rai, S. Wilser, M. Guminiak, B. Cai, and M. L. Nakarmi, Optical and electronic properties of $NiFe_2O_4$ and $CoFe_2O_4$ thin films, Appl. Phys. A **106**, 207 (2012).

[43] P. Krüger, F. Da Pieve, and J. Osterwalder, Real-space multiple scattering method for angle-resolved photoemission and valence-band photoelectron diffraction and its application to Cu(111), Phys. Rev. B **83**, 115437 (2011).

[44] Z. Novotný, G. Argentero, Z. Wang, M. Schmid, U. Diebold, and G. S. Parkinson, Ordered array of single adatoms with remarkable thermal stability: Au/Fe_3O_4(001), Phys. Rev. Lett. **108**, 216103 (2012).

[45] T. Greber, O. Raetzo, T. J. Kreutz, P. Schwaller, W. Deichmann, E. Wetli, and J. Osterwalder, A photoelectron spectrometer for *k*-space mapping above the Fermi level, Rev. Sci. Instrum. **68**, 4549 (1997).

[46] C. S. Fadley, The study of surface structures by photoelectron diffraction and auger electron diffraction, in *Synchrotron Radiation Research: Advances in Surface and Interface Science Techniques*, edited by R. Z. Bachrach (Springer, Boston, 1992), pp. 421–518.

[47] J. Osterwalder, Structural effects in XPS and AES: Diffraction, in *Surface Analysis by Auger and X-Ray Photoelectron Spectroscopy*, edited by D. Briggs and J. Grant (IM Publications and Surface Spectra Limited, Manchester, 2003), p. 557.

[48] See Supplemental Material at http://link.aps.org/supplemental/10.1103/PhysRevB.108.155403 for polarization of the

monochromatized UV source, clusters for the DOS and RSMS calculations, XPS and LEED data analyses, additional UPD measurements, PDOS and TDOS calculations, XANES and XPS data for Ni/Fe_3O_4(001) with different coverages, which includes Refs. [20,28,29,33,37,45,60,63,69].

[49] Z. Novotny, D. Aegerter, N. Comini, B. Tobler, L. Artiglia, U. Maier, T. Moehl, E. Fabbri, T. Huthwelker, T. J. Schmidt, M. Ammann, J. A. van Bokhoven, J. Raabe, and J. Osterwalder, Probing the solid-liquid interface with tender x rays: A new ambient-pressure x-ray photoelectron spectroscopy endstation at the Swiss Light Source, Rev. Sci. Instrum. **91**, 023103 (2020).

[50] C. F. Chang, Z. Hu, S. Klein, X. H. Liu, R. Sutarto, A. Tanaka, J. C. Cezar, N. B. Brookes, H.-J. Lin, H. H. Hsieh, C. T. Chen, A. D. Rata, and L. H. Tjeng, Dynamic atomic reconstruction: How Fe_3O_4 thin films evade polar catastrophe for epitaxy, Phys. Rev. X **6**, 041011 (2016).

[51] F. M. F. de Groot, M. Grioni, J. C. Fuggle, J. Ghijsen, G. A. Sawatzky, and H. Petersen, Oxygen 1*s* x-ray absorption edges of transition-metal oxides, Phys. Rev. B **40**, 5715 (1989).

[52] G. Kresse and J. Furthmüller, Efficiency of *ab-initio* total energy calculations for metals and semiconductors using a plane-wave basis set, Comput. Mater. Sci. **6**, 15 (1996).

[53] G. Kresse and J. Furthmüller, Efficient iterative schemes for ab initio total-energy calculations using a plane-wave basis set, Phys. Rev. B **54**, 11169 (1996).

[54] O. K. Andersen, Linear methods in band theory, Phys. Rev. B **12**, 3060 (1975).

[55] F. J. García de Abajo, M. A. Van Hove, and C. S. Fadley, Multiple scattering of electrons in solids and molecules: A cluster-model approach, Phys. Rev. B **63**, 075404 (2001).

[56] C. Haavik, S. Stølen, H. Fjellvåg, M. Hanfland, and D. Häusermann, Equation of state of magnetite and its high-pressure modification: Thermodynamics of the Fe-O system at high pressure, Am. Mineral. **85**, 514 (2000).

[57] S. Hüfner, *Photoelectron Spectroscopy*, Springer Series in Solid-State Sciences Vol. 82 (Springer, Berlin, 1995).

[58] J. Osterwalder, T. Greber, P. Aebi, R. Fasel, and L. Schlapbach, Final-state scattering in angle-resolved ultraviolet photoemission from copper, Phys. Rev. B **53**, 10209 (1996).

[59] D. Ihle and B. Lorenz, Small-polaron band versus hopping conduction in Fe_3O_4, J. Phys. C: Solid State Phys. **18**, L647 (1985).

[60] A. P. Grosvenor, B. A. Kobe, M. C. Biesinger, and N. S. McIntyre, Investigation of multiplet splitting of Fe 2*p* XPS spectra and bonding in iron compounds, Surf. Interface Anal. **36**, 1564 (2004).

[61] P. S. Miedema and F. M. de Groot, The iron *L* edges: Fe 2*p* x-ray absorption and electron energy loss spectroscopy, J. Electron Spectrosc. Relat. Phenom. **187**, 32 (2013).

[62] C. Chinnasamy, A. Narayanasamy, N. Ponpandian, R. Justin Joseyphus, B. Jeyadevan, K. Tohji, and K. Chattopadhyay, Grain size effect on the Néel temperature and magnetic properties of nanocrystalline $NiFe_2O_4$ spinel, J. Magn. Magn. Mater. **238**, 281 (2002).

[63] P. K. J. Wong, W. Zhang, K. Wang, G. van der Laan, Y. Xu, W. G. van der Wiel, and M. P. de Jong, Electronic and magnetic structure of C_{60}/Fe_3O_4(001): A hybrid interface for organic spintronics, J. Mater. Chem. C **1**, 1197 (2013).

[64] M. Lenglet, A. D'huysser, J. Bonelle, J. Dürr, and C. Jørgensen, Analysis of x-ray Ni Kβ emission, xanes, xps, Ni 2p, and optical spectra of nickel(II) spinels and structure inference, Chem. Phys. Lett. **136**, 478 (1987).

[65] S. Zhou, K. Potzger, Q. Xu, K. Kuepper, G. Talut, D. Markó, A. Mücklich, M. Helm, J. Fassbender, E. Arenholz, and H. Schmidt, Spinel ferrite nanocrystals embedded inside ZnO: Magnetic, electronic, and magnetotransport properties, Phys. Rev. B **80**, 094409 (2009).

[66] M. Sassi, C. I. Pearce, P. S. Bagus, E. Arenholz, and K. M. Rosso, First-principles Fe $L_{2,3}$-edge and O *K*-edge XANES and XMCD spectra for iron oxides, J. Phys. Chem. A **121**, 7613 (2017).

[67] Z. Y. Wu, S. Gota, F. Jollet, M. Pollak, M. Gautier-Soyer, and C. R. Natoli, Characterization of iron oxides by x-ray absorption at the oxygen *K* edge using a full multiple-scattering approach, Phys. Rev. B **55**, 2570 (1997).

[68] M. Taskin, Z. Novotny, N. Comini, J. T. Diulus, M. Hengsberger, and J. Osterwalder, Data set for "Surface electronic structure of Ni-doped Fe_3O_4(001)", Zenodo, https://doi.org/10.5281/zenodo.8278025 (2023).

[69] K. Momma and F. Izumi, *VESTA 3* for three-dimensional visualization of crystal, volumetric and morphology data, J. Appl. Crystallogr. **44**, 1272 (2011).